DTU Library

Numerical Modelling for the Effect of Metalmould Air Gaps on Shell Thickness in Horizontal Continuous Casting of Cast Iron

Chawla, A.; Tiedje, N.S.; Spangenberg, J.

Link back to DTU Orbit

ARCHIVES

of

FOUNDRY ENGINEERING

Numerical Modelling for the Effect of Metal-mould Air Gaps on Shell Thickness in Horizontal Continuous Casting of Cast Iron

A. Chawla * , N.S. Tiedje , J. Spangenberg

Technical University of Denmark, Denmark
* Corresponding author: Email address: ashch@dtu.dk

Abstract

This paper presents a numerical model for the horizontal continuous casting of cast iron (HCCCI). A computational three-dimensional (3D) steady-state, coupled with fluid flow and heat transfer simulation model was developed and validated against experimental results to study the shell thickness and solidification of ductile cast iron. The study introduces the influence of an air gap at the melt-mould interface, which has long been known to have a detrimental effect on the efficiency of the process. The effect of the length and thickness of the melt-mould air gaps (also referred to as top air gaps) on solidification and remelting of the solid strand is studied. Parametric studies on top air gaps suggested a substantial effect on the solid and eutectic area at the top-outlet end of the die when the length of air gas was varied. This study serves to create a foundational and working model with the overall objective of process optimisation and analyzing the effect of operating process input parameters on the shell thickness of the strand.

Keywords: Horizontal continuous casting, Cast iron, Process modelling, Air gaps

1. Introduction

With the advent of high-performance computing combined with the increased availability of data in manufacturing industries, the role of computational models has become more significant than ever for understanding and analyzing process performance, designing, optimizing, and robustness of the manufacturing process. Today, complex manufacturing processes are often addressed with multi-physics models involving numerical heat transfer, computational fluid dynamics (CFD) and computational solid mechanics along with thermodynamic and kinetic models [1-2]. CFD has been extensively used in metal casting and simulating the flow of molten metals in molds [3-5]. The multi-physics involved in horizontal continuous casting (HCC) of cast iron (CI) are complex, non-linear, and exhibit thermal, flow, metallurgical,

kinetic, hydrodynamic, and thermo-mechanic effects for a given solidification of a casting process [6].

Continuous casting is a form of permanent mold process whereby molten metal is solidified into a semi-finished billet, bloom, or slab for subsequent processing and can be employed for both ferrous and non-ferrous metals [7]. Horizontal continuous casting, one kind of continuous casting, is a promising and efficient method of producing near-net-shape, high-quality, ferrous cast products (e.g., grey, ductile, and Ni-resist irons and steel), as well as nonferrous alloys (e.g., aluminium and copper). The principal advantage of the continuous casting method, besides energy savings, and a convenient ready-to-machine form, is that CI with a finer and denser graphite structure is produced [8]. Also, the process has a 92% to 95% casting yield, because it eliminates traditional feeder needs. By maintaining an adequate balance among the metal chemistry, temperature, melt level in the receiver,

and the drawing and cooling parameters, it is possible to produce defect-free, high-quality continuous-cast bars [6-9].

Historically, the process of HCCCI is relatively new, originally developed in Europe after World War II as an alternate method of producing CI bar stock without patterns and conventional molding methods and was first installed commercially in the USA, at Wells Manufacturing Co. in 1962 [10]. In specialized continuous casting plants, liquid metal is prepared in a central melting plant from which it is distributed to several casting units. Water-cooled graphite or copper die is attached to the receiver, and a bar is pulled out by an extraction system, which controls stroke length and frequency. A special mechanism cuts and breaks the bars to required lengths. Liquid metal in the receiver plays the role of a preheated riser that continuously supplies liquid metal to feed the bar during solidification [6-9].

There are several mathematical models available in the literature for the solidification of HCC of steel via individual or a combination of fluid, thermal and mechanical modelling [11-18]. However, such knowledge is not available for CI. There are previous studies on CI modelling by Zhang, Thompson, and Croft [19-21] attempts to understand the interfacial heat transfer coefficient between the metal and the mold in a 2D study, where the studied heat transfer mechanism was conduction only. Lerner [22] proposes a systemic modelling method and attempts to understand the HCC process as a whole, and to do process optimization through solidification modelling of HCC ductile iron bars. In general, the mentioned models have assumed heat transfer effects only as it solves their problem statement and does not couple with the fluid flow because of complications and high computational requirements [23].

The formation of air gaps in the horizontal continuous casting process at the metal-mould interface is an undesired but commonly observed phenomenon [24]. The development of these gaps has been extensively studied through thermomechanical modelling for various alloys. These air gaps primarily arise when the thickness of the solidified shell increases, which then contracts away from the mould wall. This happens as a result of net thermomechanical stresses and is a function of multiple factors, of which some of the major ones are shrinkage, ferrostatic pressure of the molten core, pulling speed, superheat, and several other complex mechanisms [25-28]. The air gaps act as a thermal resistance to the flow of heat from the molten metal, thus limiting the solidification in the mould. In extreme cases, in a practical working foundry, this limiting effect can very well be the cause of a burst-out, resulting in the shutdown of the production activities [29].

The overall objective behind this study is to perform process optimisation for the HCCCI unit at Tasso A/S. The process optimisation deals with mapping the relationship between operating input process parameters such as melt velocity, inlet melt temperature, and water flowrate to the solidification of outside shell. However, in order to produce such mapping, a fast yet simple working model that can resemble the real-world as close as possible was produced to study the trends of the input parameters on the solidification. Therefore, the objective for this particular study is to establish a model that would have the most precise top air gap formations, which is then used as the base model for process optimisation studies. Furthermore, the study also addresses the effect of length and thickness of top air gaps on the solid, austenitic, and eutectic shell thickness.

The present paper presents a 3D steady-state numerical model that captures the solidification of CI in the die-casting of a horizontal continuous casting unit. The multi-physics model takes into account coupled fluid flow and heat transfer. The phase change of the alloy is integrated into the model through heat release over specific temperature spans. The simulations are validated against experimental data from an industrial casting line, and the numerical model is exploited to study the relationship between the melt-mold air gaps and the shell thickness. The rest of the paper is organized as follows: Section 2 describes the experimental setup used to validate the model. Section 3 provides an overview of the numerical model, while the results and accompanying discussion are presented in Section 4. The conclusions are summarized in Section 5.

2. Experimental Setup

Fig. 1 schematically shows the horizontal continuous casting process at Tasso A/S, which is divided into three units. The receiver unit accepts and holds the molten CI melt from the furnaces. The inductor unit is responsible for maintaining an appropriate temperature in the receiver. The die-casting unit, highlighted in blue, is where the solidification of the melt takes place and comprises of graphite die, which is in immediate contact with cooling water (indicated as CW_out and CW_in Fig. 1). The die-casting unit represents the system boundaries for the modelling task in this study.
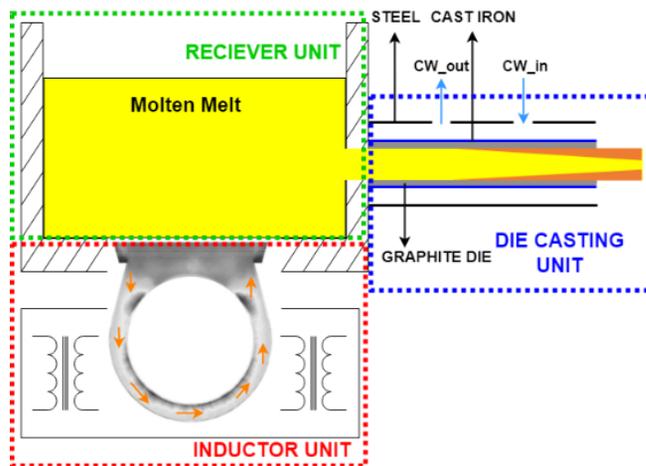

Fig. 1. Schematic of the horizontal continuous casting unit at Tasso A/S

For validation of the simulation model, experiments were set up in the die-casting unit as shown in Fig. 2 , which involved inserting sensors and recording temperatures in the graphite die. Three thermocouples were placed on both the top (1-3 in Fig. 2) and the bottom (5-7 in Fig. 2) of the die, 30 mm from the melt surface. For practical reasons, the sensors were kept 30 mm apart from each other. The sensors on top and bottom were placed 50 mm, 100mm, and 150mm into the die from the inlet of the melt. In addition, one thermocouple (4 and 8 in Fig. 2) on each side of the die was inserted 100 mm into the graphite die. The dimensions of the simulated

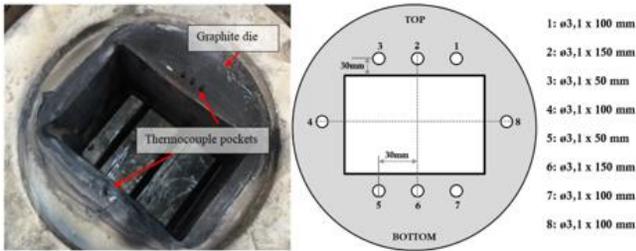section of the strand were 200 x 290 x 300 mm (height x breadth x length).

Fig. 2. Thermocouples placed in the Graphite Die

3. Numerical Model

3.1. Governing Equations

In this study, the solidification of molten melt in the graphite die was addressed by modelling the fundamental principles of integrated fluid flow and heat transfer for the entire die-casting unit. The model adopted the following assumptions:

1. The CI was modelled as an incompressible (i.e., constant density) Newtonian fluid, such that the mass conversation translates into volume conversation.
2. The effects of gravity, volume force, surface tension, and thermal radiation are not taken into account.
3. The thermo-physical properties are constant except for the specific heat.
4. No shrinkage or contraction of the metal is considered in the model.
5. Liquid metal continues to exhibit the properties of liquid below the solidus temperature T_S, thus heat transfer from the solidified shell is the same as the heat transfer from the liquid melt.
6. The process does not change with time (i.e., runs in steady-state)

In regard to the above assumptions, the velocity and temperature fields can be found by considering the following governing equations, which dictate the conservation of mass, momentum and energy:

$$\nabla \cdot (\vec{U}) = 0 \tag{1}$$

$$\nabla \cdot (\rho \vec{U}) = -\nabla p + \mu \nabla^2 \vec{U} + \vec{F}_B \tag{2}$$

$$\nabla \cdot \left((\rho C_p) \vec{U} T \right) = \nabla \cdot (k \nabla T) \tag{3}$$

$$\nabla^2 T_s = 0 \tag{4}$$

Where ρ is the density, $\vec{U}$ is the velocity vector, p is the pressure, μ is the viscosity, $\vec{F}_B$ is the body force, T is the temperature, k is the thermal conductivity, and T_s is the solid temperature. The specific heat, C_P, in Equation 3 is modelled as the sum of specific and latent heat in the phase change region [30]. The

latent heat released in the different phases, demarcated by temperatures as shown in Table 1, is evaluated by calculating the change in fraction of solid as given by Equation 5, which in turn is given by the Lever Rule [31]

$$\frac{df_S}{dT} = \frac{(T_o - T_M)}{(1-k)(T_M - T)^2} \tag{5}$$

Where f_s is the solid fraction, T_o is the liquidus temperature and T_M is the melting point of the pure CI. The range of temperatures and latent heat emitted in the two phases are provided in Table 1. These temperatures are available from the cooling curve taken as part of the foundry's quality assurance procedure using the ITACA system [32].

The rationale for not choosing a constant velocity of melt across at any cross-section of the die, and instead, solving the flow field is because the Prandtl Number is in the range of 0.3 to 1.5, which means a comparable convective and conductive heat transfer mechanism is active [33]. Since the convective heat transfer is the result of the flow field, it becomes important to solve the flow to get the temperature gradients. Furthermore, the fluid flow entering the system is affected by many things: inlet flow rate, movement of the solid shell, natural convection, solidification, and shrinkage [23].
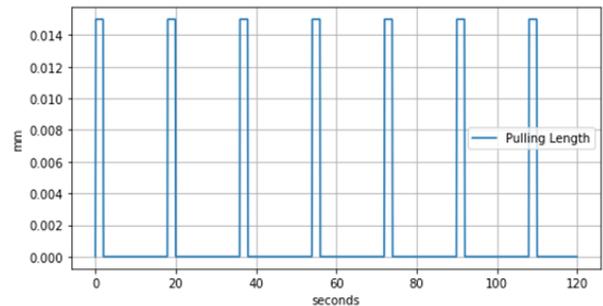

Fig. 3. Pulling parameters for a respective production day

The melt velocity $\vec{U}$ is modelled as a steady-state velocity as shown in Equation 5 and Equation 6, which in practice is a function of the pulling parameters, namely pulling length and pulling interval [34]. An example as shown in Fig. 3 displaying the pulling parameters for a respective production day, wherein the strand is being pulled 15 mm every second for 2 seconds followed by a stationary strand (0mm pull) for the next 16 seconds.

$$t_c = \frac{L}{v_t} + \left(1 + \frac{t_p}{t_D}\right) \tag{6}$$

$$\vec{U} = \frac{L}{t_c} = \left(1 + \frac{v_t}{\left(1 + \frac{t_p}{t_D}\right)}\right) \tag{7}$$

Where L is the length of the Graphite die; v_t is pulling velocity of the strand; is pause duration; t_d is drawing duration; t_c is duration of the strand in the die.

3.2. Model setup

The governing equations are solved using a finite volume-based computational fluid dynamics solver in Ansys Fluent [35]. The software has previously with success been applied to simulate other manufacturing processes such as tape casting [36-37] and additive manufacturing [38-40] A coupled pressure-velocity algorithm is applied to solve the governing equations. A second-order discretization scheme is adopted for the pressure equation, and a second-order upwind scheme is employed for the discretization of momentum and energy equations.

The die-casting unit is modelled as a 3-dimensional problem and is meshed using approximately 10 million tetrahedron cells in the entire domain, see the model in Fig. 4. The fluid flow in the melt domain is modelled as a laminar flow and the water domain is simulated as a turbulent flow as per their respective Reynolds number [41]. The heat transfer throughout the die is modelled, coupled with the heat transfer and the latent heat of solidification. Conjugate heat transfer is modelled through boundary coupling of solid/fluid and solid/solid regions [35].
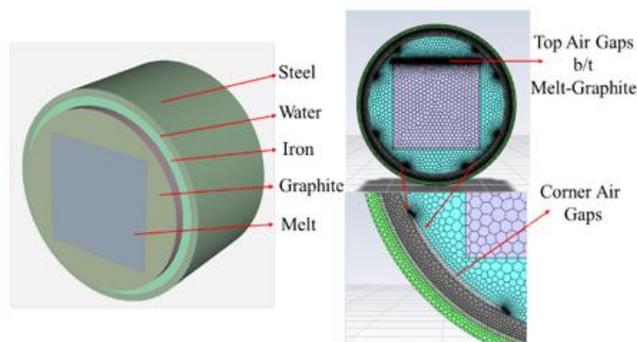

Fig. 4. Geometric Visualization of the Model with Corner and Top Air Gaps

The inlet boundary conditions imposed for the melt and water domains were velocity and mass flow, whereas pressure outlet boundary conditions were imposed on the same. The liquid adheres to the solid surfaces with a no-slip condition. All external walls exposed to the atmosphere have been assigned a zero heat flux condition, such that the total system is adiabatic.

Table 1 and Table 2 present all thermo-physical properties and process parameters used in the simulations, respectively.

Table 1.
Thermophysical properties. Sourced from [42] except T_L, $T_{e,S}$, and T_S which were obtained from the ITACA system [32].

Thermophysical Properties					
Property	Symbol	Units	Melt	Water	Air
Density	ρ	kg/m3	7000	998.2	1.225
Specific Heat	C_p	J/kgK	850	4182	1006.43
Thermal Conductivity	k	W/mK	33	0.6	0.0242
Viscosity	μ	kg/ms	0.01003	0.001003	1.7894e-05
Total Latent Heat	L	J/kg	230000	-	-
Latent Heat in Austenitic Phase	T_L to $T_{e,S}$	J/kg	17% of L	-	-
Latent Heat in Eutectic Phase	$T_{e,S}$ to T_S	J/kg	83% of L	-	-
Liquidus Temperature	T_L	°C	1185	-	-
Equilibrium Start Temp	$T_{e,S}$	°C	1145	-	-
Solidus Temperature	T_S	°C	1100	-	-

Table 2.
Simulation Process parameters.

	Units	Melt	Water
Inlet Velocity	mm/s	2	-
Inlet Temperature	°C	1230	38
Inlet Mass Flowrate	Kg/s	-	2

3.3. Air gaps

Air gaps exist by design at the corners of the graphite die, both at the top and bottom, where it meets the cooler to avoid the excess corner cooling, see Fig. 4. In addition, air gaps are formed at the top metal-mould interface towards the outlet of the die. In practice, the length of the air gaps is not constant but varies continuously according to the operational pulling length and waiting time.

To study the effect of the metal-mould air gaps, different models are set up as shown in Table 3. The model I is with no air gap between the metal and mould. Models (II-VI) account for different lengths of the air gap starting from the outlet/rear end of the strand and extending into the die. Model VII presents the scenario where the top corner air gaps were removed from the model. Model VIII takes into account an increased thickness of the top air gap. Model VII and Model VIII were compared with Model IV because of their equal length of air gaps.

Table 3.
Design parameters for simulation models

Simulation Model	Length of Air Gap (mm)	Thickness of Air Gap (mm)	Top Corner Air Gaps
I	0	0	Yes
II	50	1	Yes
III	75	1	Yes
IV	100	1	Yes
V	125	1	Yes
VI	150	1	Yes
VII	100	1	No
VIII	100	2	Yes

4. Results & Discussions

4.1. Temperature Fields

Fig. 5 illustrates the solidification and remelting at the central plane for the entire length of the strand for Model IV. The left image in Fig. 5 represents the temperature gradient, whereas the right image showcases the solid shell based on the temperatures. The strand was considered solidified when the temperatures are below 1100 °C. The solid shell forms a short distance into the die and continues to grow as the strand travels into the die. Until the point A in figure 5, where the airgap form on the top side of the strand, the shell grows at same rate at the top and the bottom of the strand. When the air gap is formed the heat flow on the top of the strand is reduced, leading to a partial remelting of the solid shell. This remelting initiates 20-30 mm after the top air gaps starts because the heat transfer in the air domain acts as a thermal insulator due to its low conductivity (See Table 1) and that local heat redistribution from the hot liquid core occurs because of this sudden drop in the heat flux in the immediate vicinity of the top part of the strand, as seen in Table 4.

Table 4.
Heat transfer parameters

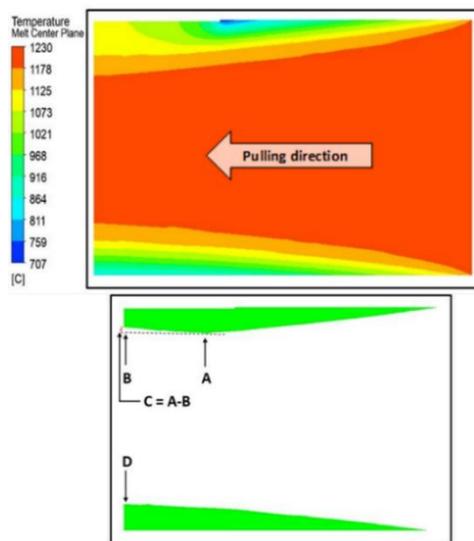| Heat Transfer Parameters	Melt-mould interface	Melt-top air gap interface
Avg. Heat Flux (KW/m2)	462	11

Fig. 5. 3D representation of solidified shell at the center (Top); 2D representation of solidified shell at the center (Bottom)
[A: Maximum Shell thickness at Melt Center - TOP.
B: Solid Shell Thickness at Outlet Melt Center - TOP.
C: Remelting.
D: Solid Shell Thickness at Outlet Melt Center – BOTTOM]

4.2. Validation Results

Fig. 6 showcases the experimental and numerical temperature at various locations in the graphite die as outlined in section 0. The measured data is representative of a production day imitating the simulation operating process conditions.

At any instant of time, the bottom temperatures were 30±5 °C higher than top temperatures at a certain cross-sectional location along the length of the die, depicting a higher cooling at the bottom. The main reason for this is because of bigger design corner air gaps at the top between the graphite die and the water cooler in comparison to the bottom between the graphite die and the water cooler as illustrated in Fig. 4. A similar trend was also seen in the simulations with higher cooling in the bottom temperatures as seen in Fig. 6.

The top and the bottom temperatures along the length of the graphite die in the experiments and simulation displayed a similar trend, with lower temperatures at 150mm and higher temperatures at 50mm, as represented by the two black dotted lines for top and bottom part of the die, respectively.

The temperatures in the simulations were constant because of their steady-state nature at any point in the die, however, the experimental temperatures varied, as seen through the box plot, because of the variation in the melt inlet temperatures. The melt inlet temperatures into the die exhibited a certain range of temperatures with the highest being at the time of pouring the melt into the receiving unit and the lowest being just before the pouring. The time between two consecutive melt pourings varied between 20-30 minutes resulting in the variation of inlet temperatures. Another different experiment [43] showed that the difference between the upper and lower limit of melt inlet temperatures to the graphite die was 14±4 °C, whereas for the simulation models the melt inlet temperatures were constant.

Furthermore, it was observed from Fig. 6 that the difference between the upper and lower limit of top temperatures was 20±5 °C, while bottom temperatures had a bigger range of 35±5 °C as can be seen in the bottom temperature box plots that have a bigger height as compared to the top temperature box plots. This is because, apart from the difference in design corner air gaps, the bottom strand carries the complete weight of the liquid metal giving a good contact between die and strand, resulting in more cooling than on the top side. The improved contact on the bottom side of the strand means that the heat transfer coefficient on that surface is larger than it is on the top side. This difference in cooling is not large, but large enough to have been captured experimentally. However, it is clear that the airgap that forms on the top side of the mould has significant influence on the thickness of the solid shell as it leaves the die. To optimize the production rate, it is imperative to understand the factors that influence the formation of the airgap.
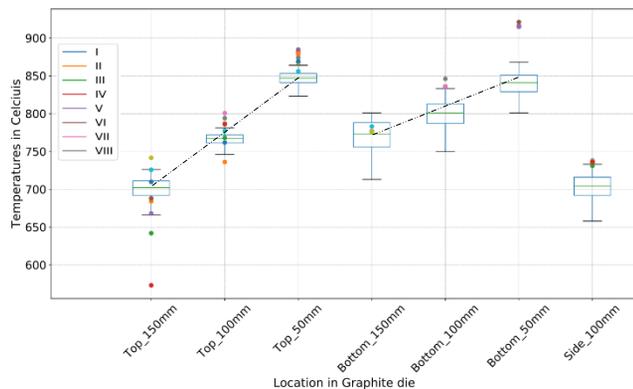
Fig. 6. Simulated and measured temperatures in a graphite die. The experimental data is presented by the box plot

4.3. Effect of Air gaps on Solid Shell Thickness and Remelting

Fig. **7** shows the top and bottom outlet shell thickness and remelting at the top. For models (I-VI), in the top part of the strand, it was observed that the remelting of the solid shell increased polynomially (order 2) when the length of the top air gaps increased from 0 to 150 mm, in increments of 25 mm, and a similar but inverse trend for outlet shell thickness. It was also observed that when the thickness of the metal mould air gap was doubled from 1mm to 2mm (Model IV vs Model VIII), there was only a marginal impact on the increase in remelting. Furthermore, it was noticed that removing the design corner air gap had a significant impact on remelting, which decreased by 35% (Model IV vs Model VII).
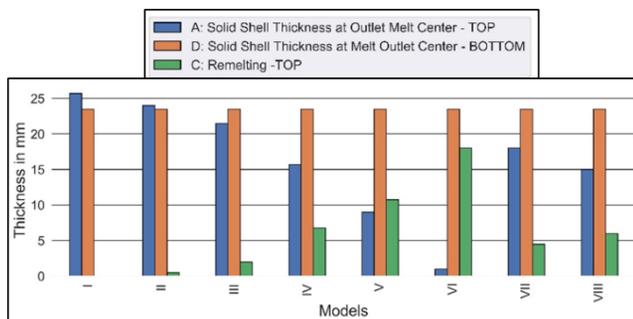

Fig. 7. Shell thickness and remelting

4.4. Effect of Air gaps on Austenitic and Eutectic Shell Thickness

Fig. 8 illustrates the division of the three CI phases - solid (green), eutectic (yellow), and austenitic (red) shell at the outlet plane of the strand for the three different lengths of the top air gaps. It was noticed that the three phases at the bottom half of the outlet plane had no impact on the size of the top air gaps. This is because the height of the strand is big enough such that the redistributed local heat fluxes established at the top do not reach the lower half. The austenitic shell thickness remained almost the same with the

increase in length of the top air gaps, however, the eutectic shell thickness doubled itself when the length of air gaps increased as seen in Fig. 8.
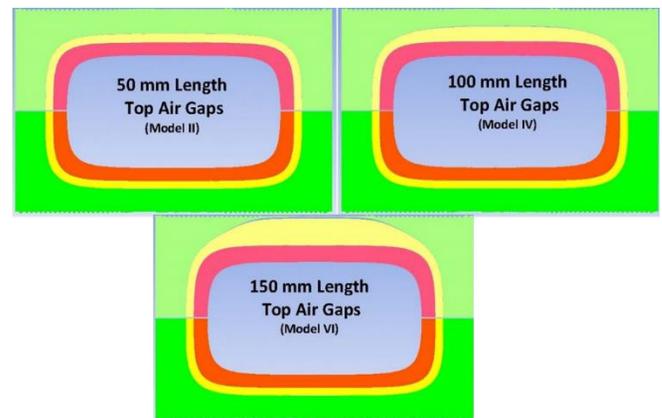

Fig. 8. Outlet plane of the strand (solid-phase: green; eutectic-phase: yellow; austenitic-phase: red)

4.5. Effect of Air Gaps on Energy

The change of shell thickness is also explicit in the results of Fig. 9, which explains the total energy leaving from the interface of the melt in the different models. It is evident from Fig. 9 that the total energy leaving the system decreases as a result of the increase in the length of the air gap. Thus, the energy leaving the melt-mould interface can be viewed as strongly correlated with the remelting of the strand.
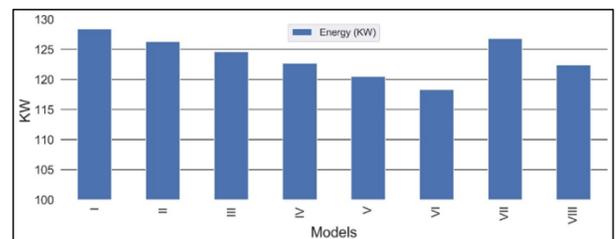

Fig. 9. Energy Leaving the Melt-Mould Boundary

4.6. Burst outs

One of the major reasons for breakouts/burst outs, which is a catastrophic phenomenon [29] can be explained through the combined effect of the decrease in solid shell thickness and an increased eutectic thickness. Furthermore, the strength of the eutectic phase is the order of a few megapascals [44] and with the static pressure acting from the height of the liquid-melt column, the likelihood of the melt escaping through the top surface of the strand increases even more potentially resulting in a burst-out and consequently stopping the production.

In this study, we have looked at where the airgap forms to investigate its effect on the shell thickness and not at how we can control the formation of the gap. Since the gap forms when the shell

is thick enough to, at least partially, hold the pressure of the melt, it should be expected that an increase in production rate will move the location of the airgap forward in the die and that a reduction in production rate will move it backwards.

By increasing the production rate, the final shell thickness at the point where the strand leaves the die will be reduced, so there is a limit to how high the rate can be to still deliver a sufficiently strong shell. On the other hand, reducing the production speed will move the airgap backwards, meaning that there can be significant remelting of the top side of the strand before it leaves the die. If remelting becomes pronounced enough to weaken the shell, it is possible that also a too low production speed will lead to burst outs.

5. Conclusions

The paper presents a numerical model within the paradigms of multi-physics modelling to simulate the solidification of CI for the horizontal continuous casting process and consequently understand the effect of metal-mould air gaps on shell thickness. The modelling of the molten melt was done through a coupled approach of fluid flow and heat transfer, and the solidification of metal was modelled in terms of temperature. The results of the simulations were validated by installing thermocouples at various locations in the graphite die for a representative production day, which showcased similar trends as in the simulations. The main conclusions derived from this study are listed as follows:

- The length of the air gap towards the outlet-top end of the die had a significant impact on the outlet shell thickness and remelting of the strand.
- The length of the air gaps was increased from 0 mm to 150 mm in increments of 25mm, which resulted in a decrease in the outlet shell thickness quadratically.
- The thickness of the air gap did not have any significant impact on the shell thickness.
- The position at which the airgap forms depend on the production process parameters (the die design, the shape of the strand, production rate and melt temperature). Understanding how these factors work to influence the location of the airgap is therefore key to optimize the output of the production.
- Furthermore, the top corner air gaps that exist by design showed a substantial decrease in remelting of the strand.

Acknowledgments

References

[1] Hattel, J.H. (2008). Integrated modelling in materials and process technology. *Materials Science and Technology.* 24(2), 137-148. https://doi.org/10.1179/174328407X236526.

[2] Sandberg, M., Yuksel, O., Baran, I., Hattel, J.H. & Spangenberg, J. (2021). Numerical and experimental analysis of resin-flow, heat-transfer, and cure in a resin-injection pultrusion process. *Composites Part A: Applied Science and Manufacturing.* 143, 106231. https://doi.org/10.1016/j.compositesa.2020.106231.

[3] Chan, K.S., Pericleous, K. & Cross, M. (1991). Numerical-Simulation Of Flows Encountered During Mold-Filling. *Applied Mathematical Modelling.* 15(11-12), 624-631. https://doi.org/10.1016/S0307-904X(09)81008-1.

[4] Mirbagheri, S.M.H., Esmaeileian, H., Serajzadeh, S., Varahram, N. & Davami, P. (2003). Simulation of melt flow in coated mould cavity in the casting process. *Journal of Materials Processing Technology.* 142(2), 493-507. https://doi.org/10.1016/S0924-0136(03)00649-6.

[5] Mirbagheri, S.M.H., Dadashzadeh, M., Serajzadeh, S., Taheri, A.K. & Davami, P. (2004). Modeling the effect of mould wall roughness on the melt flow simulation in casting process. *Applied Mathematical Modelling.* 28(11), 933-956. https://doi.org/10.1016/j.apm.2004.03.007.

[6] Lerner, V. S., & Lerner, Y. S. (2005). Solidification modeling of continuous casting process. *Journal of Materials Engineering and Performance.* 14(2), 258-262. https://doi.org/10.1361/10599490523355.

[7] Louhenkilpi, S. (2014). Continuous casting of steel. *Treatise on process metallurgy* (pp.373-434). Elsevier. DOI:10.1016/B978-0-08-096988-6.00007-9.

[8] Campbell, J. (2015). Complete Casting Handbook: Metal Casting Processes, Metallurgy, Techniques and Design: Second Edition. *Complete Casting Handbook: Metal Casting Processes, Metallurgy, Techniques and Design: Second Edition*. Elsevier Inc. https://doi.org/10.1016/C2014-0-01548-1.

[9] Stefanescu. D.M. (2017). ASM Handbook, Volume 01A - Cast Iron Science and Technology. In *Asm Handbook, Volume 01a - Cast Iron Science and Technology*. ASM International.

[10] O'Rourke, R. & Grander, M. (1999). Cast iron: a solid choice for reducing gear noise. *Gear Technology.* 16(5), 46-49.

[11] Thompson, K. & Wolf, M. (1988). The Concast heat transfer model. A proven tool for optimized slab caster design and operation. *Concast Technol. News.* 27, 6.

[12] Choudhary, S.K., Mazumdar, D. & Ghosh, A. (1993). Mathematical modelling of heat transfer phenomena in continuous casting of steel. *Isij International.* 33(7), 764-774. https://doi.org/10.2355/isijinternational.33.764.

[13] Louhenkilpi, S., Laitinen, E. & Nieminen, R. (1993). Real-time simulation of heat transfer in continuous casting. *Metallurgical Transactions B.* 24(4), 685-693. https://doi.org/10.1007/BF02673184.

[14] Bamberger, M. & Prinz, B. (1986). Mathematical-modeling of the temperature-field in continuous-casting. *Zeitschrift Fur Metallkunde.* 77(4), 234-238.

[15] Funk, G., Böhmer, J.R., Fett, F.N. & Hentrich, R. (1993). Coupled thermal and stress-strain models for the continuous

casting of steels. *Steel Research.* 64(5), 246-254. https://doi.org/10.1002/srin.199301017.

[16] Louhenkilpi, S.J. (1996). *Simulation and control of heat transfer in continuous casting of steel.* Finland: Finnish Academy of Technology.

[17] Chatterjee, A., Dutta, R., Mukhopadhyay, P.K. & Chattopadhyay, S. (1992). Heat transfer during solidification of continuously cast slabs–mathematical modelling work at tata steel. *Process Technology Conference Proceedings.* 10, 325-331.

[18] Tiedje, N. & Langer, E.W. (1993). Numerical modelling of heat transfer and solidification of continuously cast billets. *Scandinavian Journal of Metallurgy.* 22, 55-60. ISSN: 0371-0459

[19] Zhang, Y., Su, J., Zhu, J., Gan, Y., & Wang, Y. (1999). Numerical simulation on solidification process of horizontally continuously cast round iron bars. *Chinese Journal of Mechanical Engineering (English Edition).* 12(3), 204-210.

[20] Thomson, R. (1977). Notes on heat transfer and solidification rates in the continous casting of cast iron. *The British Foundryman.* 70(1), 1-7.

[21] Croft, D.R., Toothill, D., Telford, B. (1985). Heat transfer in horizontal continuous casting. In Numerical Methods in Thermal Problems, Proceedings of the Fourth International Conference, 15-18 July 1985 (pp. 1365-1376). Swansea, UK: Pineridge Press.

[22] Lerner, Y.S. (2004). Continuous casting of ductile iron. *Foundry Management and Technology.* 132(8), 40-67.

[23] Louhenkilpi, S. (2003). Modelling of heat transfer in continuous casting. *Materials Science Forum.* 414, 445-454. https://doi.org/10.4028/www.scientific.net/MSF.414-415.445

[24] Cai, Z.Z. & Zhu, M.Y. (2014). Simulation of air gap formation in slab continuous casting mould. *Ironmaking and Steelmaking.* 41(6), 435-446. https://doi.org/10.1179/1743281213Y.0000000139.

[25] G. Thomas, B., Moitra, A. & Mcdavid, R. (1996). Simulation of longitudinal off- corner depressions in continuously- cast steel slabs. *Iron and Steelmaker*. 23(4), 57-70.

[26] Cai, Z., & Zhu, M. (2014). Non-uniform heat transfer behavior during shell solidification in a wide and thick slab continuous casting mold. *International Journal of Minerals, Metallurgy, and Materials*, 21(3), 240–250.

[27] Kim, K., Han, H.N., Yeo, T., Lee, Y., Oh, K.H., & Lee, D.N. (1997). Analysis of surface and internal cracks in continuously cast beam blank. *Ironmaking & Steelmaking*. 24(3), 249-256.

[28] Han, H.N., Lee, J.-E., Yeo, T., Won, Y.M., Kim, K., Oh, K. H. & Yoon, J.-K. (1999). A finite element model for 2-dimensional slice of cast strand. *ISIJ International.* 39(5), 445-454. https://doi.org/10.2355/isijinternational.39.445.

[29] Nishida, Y., Droste, W. & Engler, S. (1986). The air-gap formation process at the casting-mold interface and the heat transfer mechanism through the gap. *Metallurgical Transactions B (Process Metallurgy).* 17(4), 833-844. DOI: 10.1007/BF02657147.

[30] Croft, D.R., Lilley, D.G. (1977). *Heat transfer calculations using finite difference equations*. United Kingdom.

[31] Fredriksson, H., & Åkerlind, U. (2006). *Materials Processing During Casting*. England: John Wiley & Sons. DOI:10.1002/9780470017920.

[32] Proservice Tech. (2019). *Thermal Analysis Software*. Retrieved June 17, 2022, from https://proservicetech.it/wp-content/uploads/2021/11/Proservicetech_Itaca_2020_Inglese_Bassa.Pdf.

[33] Incropera, F.P., DeWitt, D.P., Bergman, T.L., Lavine, A.S. (1985). *Fundamentals of heat and mass transfer*. United States of America: John Wiley & Sons.

[34] Bockus, S. (2006). Investigation of the shell solidification in horizontal continuous casting process. In *Industrial Engineering-Adding Innovation Capacity of Labour Force and Entrepreneurs: 5th International DAAAM Baltic Conference*, 20-22 April 2006 (pp.20-22). Tallinn, Estonia.

[35] Ansys, Inc. (2014). *Ansys Fluent User's Guide, Release 14.0*.

[36] Jabbaribehnam, M., Spangenberg, J. & Hattel, J.H. (2016). Particle migration using local variation of the viscosity (LVOV) model in flow of a non-Newtonian fluid for ceramic tape casting. *Chemical Engineering Research and Design.* 109, 226-233. https://doi.org/10.1016/j.cherd.2016.01.036.

[37] Jabbari, M., Baran, I., Mohanty, S., Comminal, R., Sonne, M. R., Nielsen, M.W., Spangenberg, J. & Hattel, J.H. (2018). Multiphysics modelling of manufacturing processes: A review. *Advances in Mechanical Engineering*, 10(5), 1-31. https://doi.org/10.1177/1687814018766188.

[38] Comminal, R., Serdeczny, M.P., Pedersen, D.B. & Spangenberg, J. (2018). Numerical modeling of the material deposition and contouring precision in fused deposition modeling. In *Annual International Solid Freeform Fabrication Symposium*, (pp. 1855-1864). University of Texas at Austin.

[39] Serdeczny, M.P., Comminal, R., Pedersen, D.B. Spangenberg, J. (2018). Numerical prediction of the porosity of parts fabricated with fused deposition modeling. In *Annual International Solid Freeform Fabrication Symposium,* (pp. 1849-1854). University of Texas at Austin.

[40] Serdeczny, M.P., Comminal, R., Pedersen, D.B. Spangenberg, J. (2018). Numerical study of the impact of shear thinning behaviour on the strand deposition flow in the extrusion-based additive manufacturing. In *Proceedings of the 18th International Conference of the European Society for Precision Engineering and Nanotechnology,* June 2018 (pp.283-284). Venice, Italy

[41] McCabe, W.L., Smith, J.C., Harriott, P. (1985). *Unit operations of chemical engineering*. McGraw-Hill.

[42] Valencia, J.J., Quested, P.N. (2013). Thermophysical properties. *ASM Handbook, Casting. 15* (pp. 468-481). ASM International. DOI: 10.1361/asmhba0005240.

[43] Heraeus. (n.d.). *Continuous temperature mesurement in liquid steel*. Retrieved May 27, 2022, from https://www.heraeus.com/media/media/hen/doc_hen/sensors_and_probes/cas-temp.pdf.

[44] Stefanescu, D.M. (1988). Solidification of eutectic alloys: Cast Iron. *ASM Handbook.* 15, 168-181.